MNRAS **000**, 1–15 (2016) Preprint 6 July 2016 Compiled using MNRAS LATEX style file v3.0

ExoMol molecular line lists - XVII The rotation-vibration spectrum of hot SO_3

Daniel S. Underwood[1], Sergei N. Yurchenko[1], Jonathan Tennyson[1⋆], Ahmed F. Al-Refaie[1], Sønnik Clausen[2] and Alexander Fateev[2]
[1] *Department of Physics and Astronomy, University College London, London WC1E 6BT, UK*
[2] *Technical University of Denmark, Department of Chemical and Biochemical Engineering, Frederiksborgvej 399, 4000 Roskilde, Denmark*

arXiv:1607.01242v1 [astro-ph.EP] 5 Jul 2016

Accepted XXXX. Received XXXX; in original form XXXX

ABSTRACT
Sulphur trioxide (SO_3) is a trace species in the atmospheres of the Earth and Venus, as well as well as being an industrial product and an environmental pollutant. A variational line list for $^{32}S^{16}O_3$, named UYT2, is presented containing 21 billion vibration-rotation transitions. UYT2 can be used to model infrared spectra of SO_3 at wavelengths longwards of 2 μm ($\nu < 5000$ cm^{-1}) for temperatures up to 800 K. Infrared absorption cross sections are also recorded at 300 and 500 C are used to validate the UYT2 line list. The intensities in UYT2 are scaled to match the measured cross sections. The line list is made available in electronic form as supplementary data to this article and at `www.exomol.com`.

Key words: molecular data; opacity; astronomical data bases: miscellaneous; planets and satellites: atmospheres

1 INTRODUCTION

SO_3 known to exist naturally in the Earth's atmosphere; its main source being volcanic emissions and hot springs (Michaud et al. 2005) but it also plays role in the formation of acid rain. The oxidisation of SO_2 to SO_3 in the atmosphere, followed by subsequent rapid reaction with water vapour results in the production of sulphuric acid (H_2SO_4) (Calvert et al. 1985) with many adverse environmental effects (Vahedpour et al. 2011; Kolb et al. 1994; Srivastava et al. 2004). So SO_3 is a natural product whose concentration in the atmosphere is significantly enhanced by human activity, particularly as a byproduct of industrialisation. SO_3 is observed in the products of combustion processes (Srivastava et al. 2004; Hieta & Merimaa 2014) and selective catalytic reduction (SCR) units, where the presence of both is undesirable within flue gas chambers in large quantities, as well as other industrial exhausts (Rawlins et al. 2005; Fleig et al. 2012). The control of these outputs is therefore of great importance. The spectroscopic study of sulphur oxides can also provide insight into the history of the Earth's atmosphere (Whitehill et al. 2013). All this means that observation of SO_3 spectra and hence concentrations provide a useful tool for understanding geological processes and controlling polution.

Sulphur oxide chemistry has been observed in a variety of astrophysical settings. Within the solar system, SO_3 is a constituent of the atmosphere of Venus (Craig et al. 1983; Zhang et al. 2010, 2012). Although SO_3 has yet to be observed outside our solar system, it needs to be considered alongside other sulphur oxides namely, sulphur monoxide (SO) and SO_2, which are well-known in several astronomical environments (Na et al. 1990; Petuchowski & Bennett 1992; Martin et al. 2003, 2005; Belyaev et al. 2012; Visscher et al. 2006; Belloche et al. 2013; Adande et al. 2013; Khayat et al. 2015). SO_3 chemistry has been considered in a number of enviroments including giant planets, brown dwarfs, and dwarf stars (Visscher et al. 2006). Unlike SO and SO_2, SO_3 is a symmetric species with no permanent dipole moment making it hard to detect in the interstellar medium. In practice, the identification of SO_3 in the infrared is hindered by the presence of interfering SO_2 where both species are found simultaneously; a number of their spectral features overlap, particularly the ν_3 bands of both molecules in the 1300 - 1400 cm^{-1} (7.4 μm) region. From this point of view SO_2 can also be seen as a spectral 'weed' with respect to the detection of SO_3. An understanding of the spectroscopic behaviour of both of these molecules within the same spectral window is therefore required to be able to correctly identify each species independently. In this context we note that a number of line lists are available for SO_2 isotopologues (Huang et al. 2014, 2016; Underwood et al. 2016); of particular relevence is the recent hot ExoAmes line list of Underwood et al. (2016).

The experimental spectroscopic studies of SO_3 have significant gaps, notably the absence of any measurement

⋆ Email: j.tennyson@ucl.ac.uk

© 2016 The Authors

of absolute line intensities in the infrared. This may be attributed to its vigorous chemical reactivity which make measurements difficult. SO_3 is a symmetric planar molecule with equilibrium S-O bond lengths of 1.41732 Å and inter-bond angles of 120° (Ortigoso et al. 1989), described by $\mathcal{D}_{3h}(M)$ symmetry. The ν_1, ν_2, ν_3 and ν_4 fundamental frequencies are attributed to the totally symmetric stretch at 1064.9 cm^{-1}(Barber et al. 2002), the symmetric bend at 497.5 cm^{-1}, and the asymmetric stretching and bending modes at 1391.5 and 530.1 cm^{-1}, respectively (Sharpe et al. 2003).

The infrared and coherent anti-stokes vibration-rotation spectra of a number of isotopologues of SO_3 have been extensively investigated in a series of papers by Maki and co-workers (Kaldor et al. 1973; Ortigoso et al. 1989; Chrysostom et al. 2001; Maki et al. 2001; Barber et al. 2002; Sharpe et al. 2003; Maki et al. 2004), reassessing and confirming fundamental constants and frequencies. 18 bands were analysed based on an empirical fitting to effective Hamiltonian models, yielding rovibrational constants and energy levels assigned by appropriate vibrational and rotational quantum numbers. Some temperature-dependent infrared cross sections are also available from laboratory studies (Grosch et al. 2013, 2015a), and we present new measurements in this work. Unlike all other measurements of SO_3 spectra, these cross sections are absolute. However, assigned spectra represented by line lists allow for the modelling of both absorption and emission spectra in different environments.

The "forbidden" rotational spectrum, for which centrifugal distortions can induce transitions, was investigated for the first time by Meyer et al. (1991) using microwave Fourier-transform spectroscopy. Assignments for 25 transitions were made, as well as the determination of a number of rotational constants, including the only direct measurement of the C_0 rotational constant. The work was analysed and extended theoretically (Underwood et al. 2014).

There have been a few studies on the ultraviolet spectrum of SO_3 by Fajans & Goodeve (1936), and Leroy et al. (1981), both between 220 and 270 nm where overlap with SO_2 is small. Burkholder & McKeen (1997) reported cross sections for the 195 to 330 nm range for the purposes of photolysis rate calculations of SO_3. All measurements were taken at room-temperature, and neither reported assignments for any of the bands, which exist as weak, diffuse vibrational band structures superimposed on a continuous background. As such, the rovibronic behaviour of SO_3 is much less well understood than for SO_2.

Prior to our studies, there was limited theoretical work on SO_3. Early work on anharmonic force constants (Dorney et al. 1973; Flament et al. 1992) for SO_3 led to first accurate, fully *ab initio* anharmonic quartic force field computed by Martin (1999). There have been no theoretical studies into the UV spectrum of SO_3. As for the experimental studies for SO_3, none of this work provided transition intensities. Our preliminary study for this project (Underwood et al. 2013), which produced the *ab initio*, room-temperature UYT line list, therefore provides the first absolute transition intensities for SO_3. These were used in the 2012 release of the HITRAN database (Rothman et al. 2013) to scale the relative experimental measurements allowing SO_3 to be included in the database for the first time. As discussed below, the present work suggest that these intensites may need to be reconsidered.

The present study on SO_3 was performed as part of the ExoMol project. ExoMol aims to provide comprehensive line lists of molecular transitions important for understanding hot atmospheres of exoplanets and other bodies (Tennyson & Yurchenko 2012). Besides the ExoAmes SO_2 line list mentioned above, ExoMol has produced very extensive line lists for a number of polyatomic species including methane (CH_4) (Yurchenko & Tennyson 2014), phosphine (PH_3) (Sousa-Silva et al. 2015), formaldehyde (H_2CO) (Al-Refaie et al. 2015b), hydrogen peroxide (HOOH) (Al-Refaie et al. 2015a) and nitric acid (HNO_3) (Pavlyuchko et al. 2015b). These line lists, all of which contain about 10 billion distinct vibration-rotation transitions, required the adoption of special computational procedures to make their calculation tractable. The UYT2 SO_3 line list presented here is the largest computed so far with 21 billion lines; as SO_3 is a system comprising four heavy atoms this meant considering rotation states up to $J = 130$ as part of these calculations. These calculations therefore required further enhancement of our computational methods which are described below. The lack of measured SO_3 spectra at temperatures above 300 K on an absolute scale is clearly a problem for validating our calculations. Here we present infrared absorption cross sections for SO_3 measured at a range of temperatures up to 500 C.

The next section describes our theoretical procedures; our experiments are described in section 3. Section 4 presents the UYT2 line list. Section 5 compares the UYT2 line list with our measurements with a particular emphasis on intensity comparisons. The final section gives details on how to access the line list and our conclusions.

2 THEORETICAL METHOD

To compute a variational line list requires three components (Lodi & Tennyson 2010): a suitable potential energy surface (PES), dipole moment surfaces (DMS), and a nuclear motion program. Variational nuclear motion programs, which use basis functions to provide direct solutions of the rotation-vibration Schrödinger equation for a given PES, means that interactions between the levels associated with different vibrational states and the associated intensity stealing between these bands are automatically included in the calculation. In particular, the use of exact kinetic energy operators means that how well these effects are reproduced depends strongly on the PES used; the reader is refered to a recent study by Zak et al. (2016) for a discussion of this.

Here the nuclear motion calculations are performed with the flexible, polyatomic vibration-rotation nuclear motion program TROVE (Yurchenko et al. 2007). The *ab initio* DMS surface was adopted unaltered from our previous calculations (Underwood et al. 2013) (UYT); below we describe refinement of the PES. Both the *ab initio* PES and DMS were computed at the coupled-clusters level of theory (CCSD(T)-F12b) level of theory with appropriate triple-ζ basis sets, aug-cc-pVTZ-F12 and aug-cc-pV(T+d)Z-F12 for O and S, respectively.

The label F12 in the theoretical model denotes the use of explicitly correlated functions which are designed to ac-

celarate basis set convergence. The F12b varient is an efficient F12 implementation due to Adler et al. (2007). Use of CCSD(T)-F12b methods have been shown to give improved vibrational frequencies compared to standard CCSD(T) calculations (Martin & Kesharwani 2014) but their use for intensity calculations remains relatively untested. We return to this issue below.

2.1 Refining the Potential Energy Surface

The refinement of the *ab initio* PES involved performing a least-squares fit to empirical rovibrational energies or observed transition frequencies. The procedure follows that described elsewhere (Yurchenko et al. 2011; Yachmenev et al. 2011; Sousa-Silva et al. 2013; Yurchenko & Tennyson 2014) and is based on adding a correction, ΔV, to the *ab initio* UYT PES, which is represented by an expansion

$$\Delta V = \sum_{ijklmn} \Delta f_{ijklmn} \xi_1^i \xi_2^j \xi_3^k \xi_4^l \xi_5^m \xi_6^n \quad (1)$$

in terms of the same internal coordinates as UYT Underwood et al. (2013):

$$\xi_k = 1 - \exp(-a(r_k - r_e)), \; k = 1, 2, 3, \quad (2)$$

$$\xi_4 = \frac{1}{\sqrt{6}} (2\alpha_{23} - \alpha_{13} - \alpha_{12}), \quad (3)$$

$$\xi_5 = \frac{1}{\sqrt{2}} (\alpha_{13} - \alpha_{12}), \quad (4)$$

$$\xi_6 = \sin\rho_e - \sin\bar{\rho}, \quad (5)$$

where

$$\sin\bar{\rho} = \frac{2}{\sqrt{3}} \sin[(\alpha_{23} + \alpha_{13} + \alpha_{12})/6] \quad (6)$$

$\sin\rho_e$ is the equilibrium value of $\sin\bar{\rho}$, a is a molecular parameter, and $\Delta f_{ijk\ldots}$ are expansion coefficients. Here r_i is a bond length and α_{ij} is an interbond bond angle. Further details of this functional form and symmetry relations between $\Delta f_{ijk\ldots}$ can be found elsewhere (Yurchenko et al. 2005b; Underwood et al. 2013).

The refined potential coefficients $\Delta f_{ijk\ldots}$ were determined using a least squares fitting algorithm which uses the derivatives of energies with respect to $\Delta f_{ijk\ldots}$ computed via the Hellmann-Feynman theorem (Feynman 1939). The process starts by setting all $\Delta f_{ijk\ldots} = 0$. The resulting refined PES is only an 'effective' one since it depends on any approximation in the nuclear motion calculations; it is therefore dependent on the levels of kinetic energy (KE) and PES expansion, and basis set used (see below). As a result of this, improving the nuclear motion calculation may lead to worse agreement with the observations.

The experimental data for the energies is taken from the extensive high resolution infrared studies of Maki and co-workers (Kaldor et al. 1973; Ortigoso et al. 1989; Chrysostom et al. 2001; Maki et al. 2001; Barber et al. 2002; Sharpe et al. 2003; Maki et al. 2004). The majority of these studies provide upper and lower energy states labelled by their vibrational normal mode and rotational (J, K) quantum numbers, which were validated using effective Hamiltonians. However, the bands studied by Maki et al. (2004) label transitions by rotational and vibrational quantum numbers, but do not list upper and lower energy levels. Combination differences were used to obtain energies for these bands using the experimental line positions reported by the accompanying publications; these are highlighted in Table 1. In matching experimental and computed energies, a number of experimentally derived energies were not included in the fit; these correspond to transitions excluded by Maki *et al.* from their Hamiltonian fits. A total of 119 energy levels for $J \leq 5$ were chosen from this set based on their reliability at reproducing the observed transitions, with the condition that they are physically accessible states with A' or A'' symmetry; any published values of experimentally-derived purely vibrational terms (i.e. band centres) that are inaccessible were not included. Table 3 lists all the $J = 5$ levels used in the refinement process, comparing with their final computed counterparts.

Table 1. Comparison of RMS differences for the *ab initio* (UYT) and refined (UYT2) PES for observed vibrational band centres of SO_3. Values for band centres are the experimental ones of (Maki et al. 2001). All values are in cm^{-1}. Note: UYT does not cover transition frequencies above 4000 cm^{-1}.

Band	Band Centre	UYT	UYT2
$2\nu_2$ - ν_2	497.45	0.73	0.09
ν_2 - ν_0	497.57	0.77	0.05
$\nu_2 + \nu_4$ - ν_4	497.81	0.82	0.03
$2\nu_4^{(l_4=0)}$ - ν_4	529.72	1.33	0.30
ν_4 - ν_0	530.09	1.41	0.09
$\nu_2 + \nu_4$ - ν_2	530.33	0.22	0.08
$2\nu_4^{(l_4=2)}$ - ν_4	530.36	1.54	0.37
ν_1 - ν_4	534.83	0.47	0.20
ν_3 - ν_0	1391.52	4.06	0.09
$2\nu_2 + \nu_4$ - ν_0	1525.61	0.19	0.08
§$\nu_2 + 2\nu_4^{(l_4=0)}$ - ν_0	1557.88	2.39	1.17
§$\nu_2 + 2\nu_4^{(l_4=2)}$ - ν_0	1558.52	2.12	0.64
§$\nu_1 + \nu_2$ - ν_0	1560.60	1.14	1.28
§$3\nu_4^{l_4=1}$ - ν_0	1589.81	6.73	4.00
§$\nu_1 + \nu_4^{(l_4=1)}$ - ν_0	1593.69	3.32	3.57
⋆§$(\nu_3 + \nu_4)^{(L=2)}$ - ν_0	1917.68	5.34	0.65
$2\nu_3^{(l_3=2)} - \nu_0$	2777.87	7.53	0.20
§$3\nu_3^{(l_3=1)}$ - ν_0	4136.39	–	0.08

⋆The value L is given by $L = |l_3 + l_4|$, see Maki et al. (2004).
§These bands are refined using energy levels obtained from the data by (Maki et al. 2001, 2004) via combination differences.

Table 1 shows the effect of the final potential refinement on the bands used in the refining procedure. The root mean square (RMS) differences are calculated by matching all experimental lines for each band with calculated values via their quantum number assignments for all $J \leq 5$ available.

The RMS differences calculated are slightly increased when including higher $J > 5$ term values comparing to the residuals in Table 3 for a few bands as a result of the refinement, namely the $\nu_1 + \nu_2$ and $\nu_1 + \nu_4^{(l_4=1)}$ bands. The experimental energy levels used to refine these two bands were obtained using combination differences. However, for some rotationally excited levels within these bands, the quantum number labelling of the experimental transitions appears dubious: in particular there are a number of transition whose labels are duplicated. These transitions were not included in the RMS difference calculations but there must be some doubt about the validity of the quantum number assignments of the other transitions in these bands. This may well explain the increased the RMS difference.

Table 2. Comparisons of vibrational ($J = 0$) terms for SO_3, between experimental values (Maki et al. 2001), and the *ab initio* (UYT) and refined (UYT2) PES. All values are given in cm^{-1}.

	Obs.	UYT	UYT2
ν_2	497.57	498.48	497.56
ν_4	530.09	528.59	530.09
$2\nu_2$	995.02	995.35	993.67
$\nu_2 + \nu_4^{(l_4=1)}$	1027.90	1027.35	1027.33
$2\nu_4^{(l_4=0)}$	1059.81	1056.50	1059.48
$2\nu_4^{(l_4=2)}$	1060.45	1057.38	1060.45
ν_1	1064.92	1065.75	1066.49
ν_3	1391.52	1387.45	1391.51
$3\nu_2$	1492.35	1490.76	1488.47
$2\nu_2 + \nu_4^{(l_4=1)}$	1525.61	1524.48	1524.20
$\nu_2 + 2\nu_4^{(l_4=0)}$	1557.88	1555.59	1557.50
$\nu_2 + 2\nu_4^{(l_4=2)}$	1558.52	1556.45	1558.46
$\nu_1 + \nu_2$	1560.60	1565.33	1565.07
$3\nu_4^{(l_4=1)}$	1589.81	1586.46	1588.97
$3\nu_4^{(l_4=3)}$	1591.10	1586.43	1591.06
$\nu_1 + \nu_4^{(l_4=1)}$	1593.69	1593.36	1595.92
$\nu_2 + \nu_3^{(l_3=1)}$	1884.57	1881.53	1884.29
$^\star(\nu_3 + \nu_4)^{(L=2)}$	1917.68	1912.24	1917.68
$^\star(\nu_3 + \nu_4)^{(L=0)}$	1918.23	1914.56	1919.63
$2\nu_3^{(l_3=0)}$	2766.40	2759.12	2766.38
$2\nu_3^{(l_3=2)}$	2777.87	2770.29	2777.86
$3\nu_3^{(l_3=1)}$	4136.39	4126.78	4136.33

*The value L is given by $L = |l_3 + l_4|$, see Maki et al. (2004).

Table 2 compares all published vibrational ($J = 0$) term values with those calculated with TROVE before and after refinement. There are some discrepancies introduced by the refinement procedure and in some cases deteriorations from the pre-refined values (e.g $2\nu_2$). The quality of the refinement can be assessed from Table 1, with the exception of $3\nu_2$, for which there is no experimental band data available beyond the quoted vibrational term value (Maki et al. 2004).

Our refined PES is given as Supplementary Information to this article.

2.2 Calculation using TROVE

In specifying a calculation using TROVE, it is necessary to fix a number of parameters. In particular both the KE and PES are expanded as a Taylor series about the equilibrium geometry (Yurchenko et al. 2007). For UYT the expansions were truncated at 4^{th} and 8^{th} orders respectively. Here the KE expansion order was increased to 6^{th} in order to allow better convergence. For the detailed description of the basis set see Underwood et al. (2013). Here it suffices to define the maximal polyad number $P_{\max}$ used in TROVE to control the size of the basis set. The polyad number in case of SO_3 in terms of the normal mode quantum numbers is given by

$$P = 2(n_1 + n_3) + n_2 + n_4, \tag{7}$$

where n_1, n_2, n_3 and n_4 are the normal mode quanta associated with the ν_1, ν_2, ν_3 and ν_4 vibrational modes. For the UYT2 calculations the value of $P_{\max}$ was set initially to 24 for the 1D primitive basis functions to form a product-type basis set, which was then contracted to $P_{\max} = 18$ after a set of prediagonalizations of reduced Hamiltonian matrices and symmetrized. The value of $P_{\max}$ used for UYT was 12. This increase was necessary to allow both better convergence of the increased number of energies which is needed for high temperature spectra. Only energies lying up to 10 000 cm^{-1} above the ground state were considered as part of this study.

Table 3. Observed (Maki et al. 2001) minus Calculated residuals for the $J = 5$ energy levels used in the refinement procedure. All values are in cm^{-1}. The corresponding values for $J \leq 5$ are given in Underwood (2016).

State	K	Obs.	UYT2	Obs. - Calc.
ν_0	3	8.885	8.886	-0.001
ν_2	3	506.367	506.360	0.008
	0	507.900	507.893	0.007
	5	535.323	535.312	0.011
$\nu_4^{(l_4=1)}$	4	538.471	538.490	-0.020
	2	539.561	539.560	0.001
	1	540.677	540.685	-0.008
$2\nu_2$	3	1002.357	1002.411	-0.054
$\nu_2 + \nu_4^{(l_4=1)}$	5	1033.102	1033.058	0.044
	4	1036.241	1036.226	0.016
	2	1037.252	1037.219	0.033
	1	1038.243	1038.220	0.023
	5	1068.278	1068.303	-0.025
$2\nu_4^{(l_4=0)}$	3	1068.461	1068.456	0.005
$2\nu_4^{(l_4=2)}$	2	1071.024	1071.031	-0.007
	5	1398.427	1398.437	-0.010
$\nu_3^{(l_3=1)}$	2	1401.580	1401.581	-0.001
	1	1401.599	1401.591	0.009
	5	1529.365	1529.362	0.003
$2\nu_2 + \nu_4^{(l_4=1)}$	4	1532.498	1532.520	-0.022
	2	1533.442	1533.448	-0.006
$\nu_1 + \nu_2$	3	1573.870	1573.856	0.014
	0	1575.400	1575.387	0.013
$3\nu_4^{(l_4=1)}$	4	1597.408	1597.410	-0.002
$\nu_1 + \nu_4^{(l_4=1)}$	5	1601.162	1601.150	0.012
	4	1604.308	1604.322	-0.014
	2	1605.430	1605.426	0.004
	1	1606.574	1606.577	-0.002
	5	1923.797	1923.808	-0.011
$^\star(\nu_3 + \nu_4)^{(L=2)}$	4	1925.310	1925.318	-0.008
	0	1927.488	1927.422	0.066
	1	1927.982	1927.988	-0.006
	5	2782.262	2782.227	0.035
$2\nu_3^{(l_3=2)}$	4	2786.812	2786.837	-0.025
	2	2786.901	2786.888	0.014
	1	2788.419	2788.425	-0.006
$3\nu_3^{(l_3=1)}$	5	4143.316	4143.246	0.070
	2	4146.379	4146.329	0.050

*The value L is given by $L = |l_3 + l_4|$, see Maki et al. (2004).

The high symmetry of $^{32}S^{16}O_3$, and the associated nuclear spin statistics, means that it is only necessary to consider transitions between A_1' and A_1'' symmetries of the $\mathcal{D}_{3h}$ point group used for the calculations. The final UYT2 line list consists of all allowed transitions between $0 < \nu \leq 5000$ cm^{-1}, satisfying the conditions $E' \leq 9000$ cm^{-1}, $E'' \leq 4000$ cm^{-1} and $J \leq 130$. These parameters are designed to give a complete spectrum up to 5000 cm^{-1} ($\lambda > 2$ μm) for temperatures up to about 800 K. Generating a complete line list with these parameters is computationally demanding and therefore requires special measures to be taken.

In terms of memory, diagonalisation of the Hamiltonian matrices is the most computationally expensive part

of the line list calculation. For each J, a matrix is built (Yurchenko et al. 2007, 2009) and then stored in the memory for diagonalisation, using an appropriate eigensolver routine. TROVE uses a symmetry adapted basis set representation and allows splitting of each J Hamiltonian matrix further into the six symmetry blocks (A_1', A_2', E', A_1'', A_2'', and E'') which are dealt with separately. Since only the A_1' and A_1'' symmetry species are allowed by the nuclear statistics of $^{32}S^{16}O_3$, only these symmetry blocks are diagonalized.

Memory requirements scale with the square of the dimension of the Hamiltonian matrix, $N_J^{\rm Ham}$. This is given roughly by $N_J^{\rm Ham} = N_{J=0} \times (2J+1)$, where $N_{J=0}$ is the dimension of the purely vibrational matrix. For UYT2, the combined dimension $N_{J=0}$ of both A_1' and A_1'' symmetries is 2692; for comparison, the UYT line list calculations used $N_{J=0} = 679$. The size of the largest matrix considered in the room-temperature calculations (for $J = 85$) is $N_{85}^{\rm Ham} = 111\,296$, which is already surpassed by $J = 21$ for UYT2 for which the value of $N_{85}^{\rm Ham} = 454\,488$. It became quickly apparent that the diagonalisation techniques previously employed to determine the UYT wavefunctions would be impractical for UYT2.

Nuclear motion calculations were performed using both the Darwin and COSMOS HPC facilities in Cambridge, UK. Each of the computing nodes on the Darwin cluster provide 16 CPUs across two 2.60 GHz 8-core Intel Sandy Bridge E5-2670 processors, and a maximum of 64 Gb of RAM. The advantage of moving eigenfunction calculations to the Darwin cluster are that an entire node can be dedicated to one calculation, spread across the 16 CPUs. Since multiple nodes can be accessed by a single user at any time, multiple computations were carried out simultaneously.

Diagonalisation of matrices with $J \leq 32$ was possible using the LAPACK DSYEV eigensolver (Anderson et al. 1999), optimised for OpenMP parallelisation across multiple (16) CPUs. For $32 < J \leq 90$ a distributed memory approach was used with an MPI-optimised version of the eigensolver, PDSYEVD, which allowed diagonalisations across multiple Darwin/COSMOS nodes in order to make use of their collective memory. In order to diagonalise the matrix within the 36 hour wall clock limit, it was necessary to perform this method in three steps. First, for a given J and symmetry species Γ, the Hamiltonian matrix was constructed and saved to disk. Secondly, the matrix was then read and diagonalised using PDSYEVD across the number of nodes required to store of the matrix in their shared memory. This produces a set of eigenvectors which were read in again to convert into the TROVE eigenfunction format.

For $J > 90$ yet another approach was developed for use on the COSMOS shared memory machine. This method employed the PLASMA DSYTRDX routine (Kurzak et al. 2013) and, unlike the above procedure, constructed, diagonalised and stored wavefunctions to disk in a single process by extending both the standard wallclock time and memory limits. For $J = 130$ ($\Gamma = A_1'$) a total of 52 hours of real time was taken to construct and diagonalize the Hamiltonian matrix across 416 CPUs, and utilising 3140 Gb of RAM.

While matrix diagonalisation dominates the memory requirements of the calculation, computing the line strengths, $S(f \leftarrow i)$, is the major user of computer time. In principle line strengths for all transitions obeying the rigorous electric dipole selection rules, $\Delta J = J' - J'' = 0, \pm 1$ ($J'' + J' \geq 1$) and $A_1' \leftrightarrow A_1''$, were computed. In practice this was modified to reduce the computational demands. Firstly, calculations of the line strength only take into consideration the basis functions of the final state wavefunction whose coefficients are greater than 10^{-14}. In addition to this a threshold value for the Einstein A coefficient of 10^{-74} s^{-1} dictates which transitions are kept. However, the number of line strength calculations to be performed still remains very large and even with parallelisation across multiple Darwin CPUs, performing the calculations proved to be both computationally expensive and difficult.

To help expedite these computations, an adapted version of TROVE was used which is optimised for performing calculations on graphical processing units (GPUs). The use of this implementation, known as GAIN (GPU Accelarated INtensities) (Al-Refaie et al. 2016), allowed for the computation of transition strengths for the more computationally demanding parts of the calculations. These calculations were performed on the Emerald GPU cluster, based in Southampton. In general, the calculation of transition strengths across multiple GPUs was much faster than the Darwin CPUs. For example, there are a total of 349 481 979 transitions for J'' = 35, which took a total of 17 338 CPU hours to compute on the Darwin nodes, compared to 2053 GPU hours on the Emerald nodes for 346 620 894 transitions for the larger J'' = 59 case. These GPU calculations were carried out for those $J \leftrightarrow J+1$ pairs containing a large number of states, while the Darwin CPUs were reserved for the less computationally demanding sections.

21 billion transitions were calculated for UYT2, which is two orders of magnitude larger than UYT. Overall performing the computations needed for the UYT2 line list took us over 2 years.

3 EXPERIMENTS

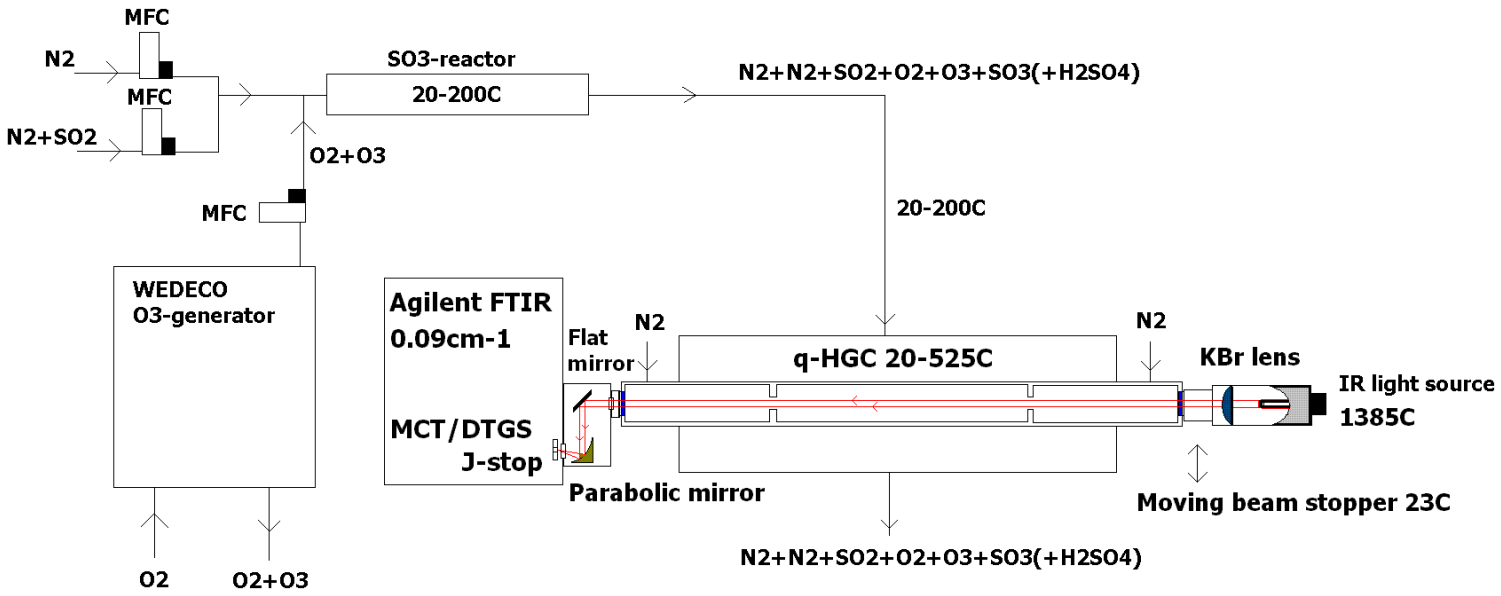

Figure 1. Set up used for $SO_2/SO_3/O_3$ infrared absorption measurements.

SO_3 absorbance measurements at temperatures up to 500 C were performed using a quartz high-temperature gas flow cell (q-HGC). The cell has been described in details by Grosch et al. (2013) and has recently been used for measurements with NH_3 (Barton et al. 2015), S-containing gases (Grosch et al. 2015a) and some PAH compounds (Grosch et al. 2015b).

Because SO_3 is an extremely reactive gas and normally contains traces of SO_2 if ordered from a gas supplier, it was decided to produce SO_3 directly in the set up. It is known that SO_2 can react with O_3 and form SO_3:

$$SO_2 + O_3 \rightarrow SO_3 + O_2. \quad (8)$$

The rate constant for the reaction (8) is temperature dependent: higher temperatures favour SO_3 formation. However at higher temperatures O_3 starts to decompose into O_2 and O:

$$O_3(+M) \rightarrow O_2 + O(+M) \quad (9)$$

Some O and O_2 can contribute further in SO_3 formation and "re-cycle" O_3:

$$\begin{aligned} SO_2 + O(+M) &\rightarrow SO_3(+M) \\ O + O_2(+M) &\rightarrow O_3(+M) \\ O + O(+M) &\rightarrow O_2(+M) \end{aligned} \quad (10)$$

If any water traces are present in the system, SO_3 will rapidly be converted into sulfuric acid (H_2SO_4):

$$SO_3 + H_2O(+M) \rightarrow H_2SO_4(+M), \quad (11)$$

which is then followed by further surface-promoted reaction:

$$H_2SO_4 + \text{surface} \rightarrow \text{products}. \quad (12)$$

Other possible SO_3 removal channels are:

$$\begin{aligned} SO_3(+M) &\rightarrow SO_2 + O(+M) \\ SO_3 + \text{surface} &\rightarrow \text{products}. \end{aligned} \quad (13)$$

These reactions are very prominent in a clean set up with "active" surfaces.

In the presence of O_2, a reversible reaction (which is also temperature-dependent) takes place:

$$2SO_2 + O_2(+M) \rightarrow 2SO_3(+M). \quad (14)$$

However SO_3 formation through reaction (14) takes place at temperatures higher than 500 C. The set-up is shown in Fig. 1. It can be divided into two parts: a SO_3 generation part and a part for optical measurements.

The optical part of the set up includes a high-resolution FTIR spectrometer (Agilent 660 with a linearized broadband MCT detector), the q-HGC and a light-source (Hawkeye, IR-Si217, 1385C) with a KBr plano-convex lens. The light source is placed in the focus of the KBr lens. The FTIR and sections between the FTIR/q-GHC and q-HGC/IR light source have been purged by CO_2/H_2O-free air obtained from a purge generator.

The O_3-generation part consists of a set of high-end mass-flow controllers (MFC's), O_3-generator and a unit called SO_3-reactor. MFC's (Bronkhorst) have been used to keep constant gas flows and mix gas flows of N_2, N_2+SO_2 and O_2+O_3 in desirable ratios. An O_3-generator (WEDECO GSO 30, water cooled, rated capacity at full load 100 g hour^{-1} of O_3 with use of O_2) was used to produce O_3 from O_2. Because of the high O_2 flow rate required for stable operation of the O_3-generator, only a part of the O_2+O_3 flow was used in the measurements. The ozone generator was operated at about 30% (225 W) of the full load. SO_3-reactor was a 50 cm heated quartz tube (20 – 200 C) with inner diameter of 50 mm. N_2+SO_2 was mixed in the SO_3-reactor with O_2+O_3 from the ozone-generator at 170 – 190 C. The gas residence time in the O_3-reactor was about 60 s at 1 l_n min^{-1} (normal litres per minute) flow rate which was enough to convert about 50% of SO_2 into SO_3 and at the same time mostly decompose O_3. The SO_3-reactor was connected through a heated Teflon-line (inner diameter 4 mm, T = 20 – 200 C) to the inlet of the q-HGC. The gas residence time in the Teflon-line was about 0.8 s (at 1 ln/min) and some further (minor) conversion of SO_2 to SO_3 took also place.

Bottles with premixed gas mixture, N_2 + SO_2 (5000ppm) (Strandmöllen) and N_2/O_2 (99.998%) (AGA) have been used for reference and SO_2/SO_3 absorbance measurements. The main flow in the q-HGC was balanced with the two buffer flows of N_2 from q-HGC's buffer parts. Most of SO_2/SO_3 absorbance measurements have performed at 0.25-0.5 cm^{-1} nominal spectral resolutions and around atmospheric pressure in the q-HGC. Few measurements have been performed at 0.09 cm^{-1} spectra resolution. The measurements were performed in following steps:

(i) N_2 + O_2 in q-HGC, reference spectra, ozone generator "off";
(ii) N_2 + O_2 + SO_2 (2500 ppm) in q-HGC, absorption spectra, ozone generator "off";
(iii) N_2 + O_2 + SO_2 + SO_3 + O_3 in q-HGC, absorption spectra, ozone generator "on", initial SO_2 concentration 2500 ppm;
(iv) N_2 + O_2 + O_3, in q-HGC, ozone generator "on" in order to measure O_3 traces in the q-HGC (addition step used only for some measurements).

O_3 has several absorption bands in 400-6000 cm^{-1}, which do not interfere with SO_2/SO_3 absorption bands. At each step two measurements were made: with a light source (emission from the cell and light source) and without a light source (emission from the cell). Experimental absorption spectra SO_2/SO_3 were reconstructed in the way described in section 3.1 of Barton et al. (2015). Spectra of SO_2 measured in step 2 have been normalized and subtracted from the composite SO_2+SO_3 spectra obtained in step 3 in order to get the zero absorption signal in vicinity of the SO_2 bands as one can see in Fig. 2. It was further assumed that all SO_2 was consumed to produce SO_3 (i.e. no SO_3 losses channels). Note various log10-absorption scales on these figures. The extra (weak) broad feature in the region 1200-1285 cm^{-1} is caused by the O_3 production in the O_3-generator.

Figure 3 gives a comparison of our newly measured cross sections in the 7.4 μm region with those available from the PNNL database for SO_2 (upper) and SO_3 (lower).

4 OVERVIEW OF THE UYT2 LINE LIST

The UYT2 line list is presented in the ExoMol format (Tennyson et al. 2013, 2016) with main data contained in a

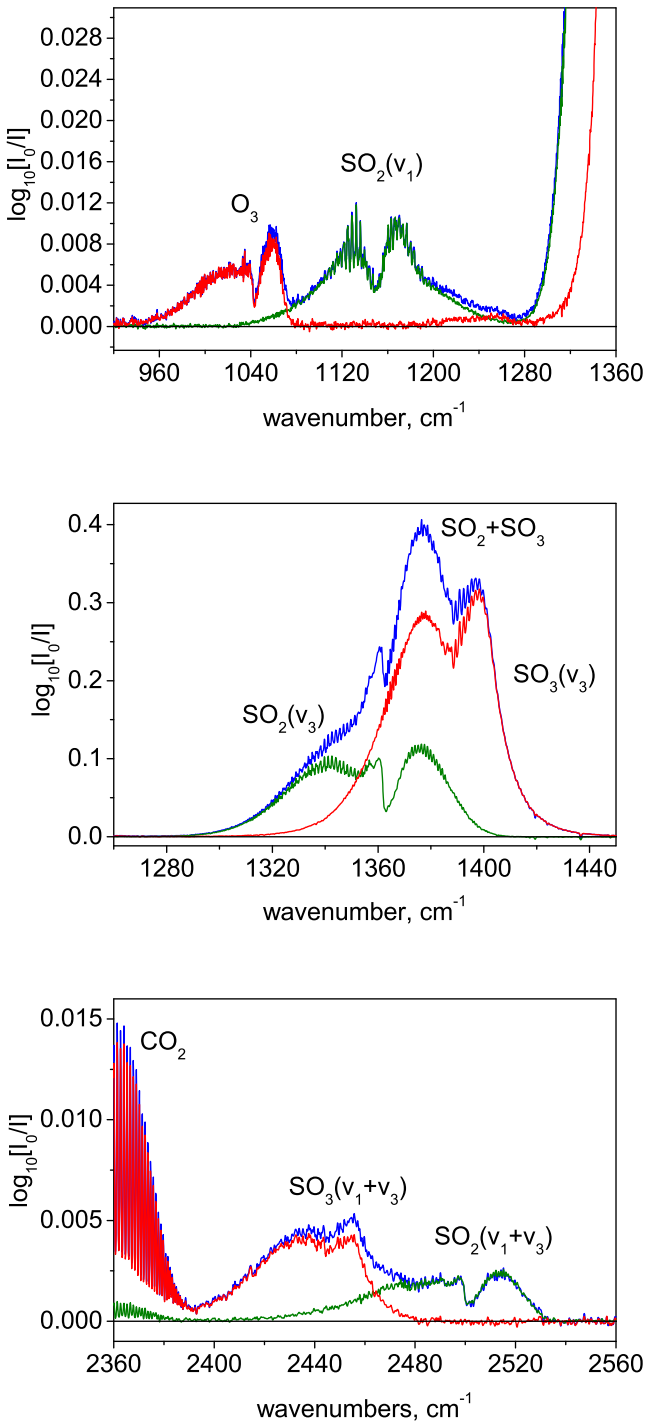

Figure 2. Composite SO_2+SO_3+O_3 absorption spectrum at 300 C (blue) together with (normalized) SO_2 spectrum (olive) and the result of subtraction of SO_2 spectrum from the composite one (red): The vicinity of the ν_1 (upper), ν_3 (middle) and $\nu_1 + \nu_3$(lower) bands of SO_2.

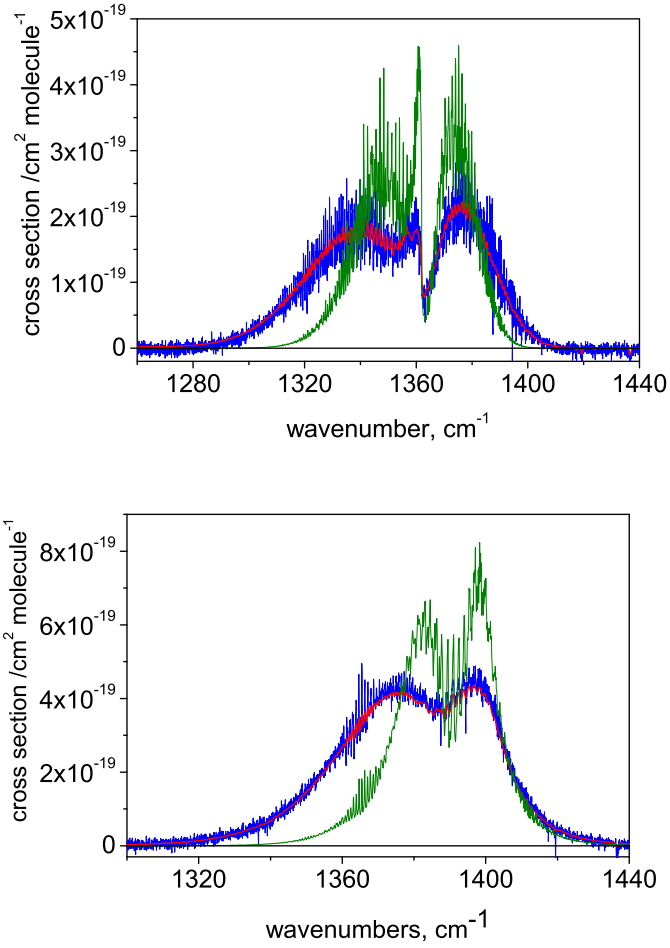

Figure 3. SO_2 (upper) and SO_3 (lower) absorption cross sections at 400 C: 0.09 cm^{-1} (blue, boxcar), 0.5 cm^{-1} (red, triangular). Cross section from PNNL database at 25 C (olive, 0.112 cm^{-1}, boxcar) are shown for comparison.

states and a set of transtions files. Tables 4 and 6 give portions of these files. The complete files can be obtained via `ftp://cdsarc.u-strasbg.fr/pub/cats/J/MNRAS/xxx/yy`, or `http://cdsarc.u-strasbg.fr/viz-bin/qcat?J/MNRAS//xxx/yy`, as well as the exomol website, `www.exomol.com`.

The energy levels listed in the states file are labelled with the quantum numbers summarised in Table 5 and are based on those recommended by Down et al. (2013) for ammonia with the simplification that one does not need to consider inversion. Only quantum numbers J, $g_{\rm Total}$, $\Gamma_{\rm Total}$ and the counting index, n are rigorously defined. The remaining quantum numbers represent the largest contribution from rotational and vibrational components of the wavefunction expansion associated with a given state. TROVE provides local mode quantum numbers associated with the basis set construction scheme used (Underwood et al. 2013). The normal mode vibrational quantum numbers, n_1, n_2, n_3 and n_4, and or their angular momentum projections $L_3 = |l_3|$ and $L_4 = |l_4|$ were obtained from the local mode quantum numbers via the correlation rules

$$n_1 + n_3 \quad = \quad v_1 + v_2 + v_3, \qquad (15)$$

Table 4. Extract from the UTY2 state file for SO_3; quantum numbers are specified in Table 5. The full table is available from http://cdsarc.u-strasbg.fr/cgi-bin/VizieR?-source=J/MNRAS/xxx/yy.

n	$\tilde{E}$	g	J	$\Gamma_{\rm Total}$	K	$\Gamma_{\rm Rot}$	v_1	v_2	v_3	v_4	v_5	v_6	n_1	n_2	n_3	L_3	n_4	L_4	$\Gamma_{\rm Vib}$
1	0.0000	1	0	1	0	1	0	0	0	0	0	0	0	0	0	0	0	0	1
2	993.6780	1	0	1	0	1	0	0	0	0	0	2	0	2	0	0	0	0	1
3	1059.4770	1	0	1	0	1	0	0	0	0	2	0	0	0	0	0	2	0	1
4	1066.4970	1	0	1	0	1	1	0	0	0	0	0	1	0	0	0	0	0	1
5	1591.0349	1	0	1	0	1	0	0	0	0	3	0	0	0	0	0	3	1	1
6	1919.6346	1	0	1	0	1	1	0	0	0	1	0	0	0	1	1	1	1	1
7	1981.9944	1	0	1	0	1	0	0	0	0	0	4	0	4	0	0	0	0	1
8	2054.0505	1	0	1	0	1	0	0	0	0	2	2	0	2	0	0	2	0	1
9	2061.9334	1	0	1	0	1	1	0	0	0	0	2	1	2	0	0	0	0	1
10	2117.4659	1	0	1	0	1	0	0	0	0	4	0	0	0	0	0	4	0	1
11	2124.4973	1	0	1	0	1	1	0	0	0	2	0	1	0	0	0	2	0	1
12	2129.3331	1	0	1	0	1	0	1	1	0	0	0	2	0	0	0	0	0	1
13	2444.1614	1	0	1	0	1	1	0	0	0	2	0	0	0	1	1	2	2	1
14	2586.0493	1	0	1	0	1	0	0	0	0	3	2	0	2	0	0	3	1	1
15	2648.2382	1	0	1	0	1	0	0	0	0	5	0	0	0	0	0	5	1	1
16	2655.7551	1	0	1	0	1	1	0	0	0	3	0	1	0	0	0	3	1	1
17	2766.3812	1	0	1	0	1	0	2	0	0	0	0	0	0	2	0	0	0	1
18	2904.3481	1	0	1	0	1	1	0	0	0	1	2	0	2	1	1	1	1	1

Table 5. Quantum numbers used in labelling energy states.

Quantum Number	Description
n	Counting index
$\tilde{E}$	Energy value ($\rm cm^{-1}$)
g	Total degeneracy of the state
J	Angular momentum quantum number
$\Gamma_{\rm Total}$	Total symmetry in $\mathcal{D}_{3h}$(M): $1 = A_1'$, $4 = A_1''$
K	Projection of J on to the z-axis
$\Gamma_{\rm Rot}$	Rotational symmetry in $\mathcal{D}_{3h}$(M): $1 = A_1'$, $2 = A_2'$, $3 = E'$, $4 = A_1''$, $5 = A_2''$, $6 = E''$
$v_i, i = 1-6$	Local mode vibrational quantum numbers
n_1, n_2, n_3, n_4	Normal mode vibrational quantum numbers
L_3, L_4	L projections of the vibrational angular momenta
$\Gamma_{\rm Vib}$	Vibrational symmetry in $\mathcal{D}_{3h}$(M): $1 = A_1'$, $2 = A_2'$, $3 = E'$, $4 = A_1''$, $5 = A_2''$, $6 = E''$

Table 6. Extract from the UTY2 transitions file for SO_3. The full table is available from http://cdsarc.u-strasbg.fr/cgi-bin/VizieR?-source=J/MNRAS/xxx/yy.

f	i	A
237007	249581	1.1253e-17
158430	148459	2.8358e-17
549592	568676	1.3725e-16
120670	112002	1.4546e-16
2080392	2117071	9.0696e-18
289088	302965	1.4938e-16
393104	377035	1.5764e-16
43637	49289	2.1375e-16
587986	607961	2.0370e-16
587868	647986	4.2068e-18
2007259	2043487	5.2490e-18
627725	648113	3.0673e-16

f: Upper state counting number; i: Lower state counting number; A_{fi}: Einstein-A coefficient in $\rm s^{-1}$.

$$n_2 + n_4 = v_4 + v_5 + v_6, \quad (16)$$

and

$$l_3 = -v_3, -v_3+2, ..., v_3-2, v_3, \quad (17)$$

$$l_4 = -v_4, -v_4+2, ..., v_4-2, v_4, \quad (18)$$

where v_1, v_2 and v_3 are three stretching, v_4 and v_5 are two deformational (asymmetric) bending and v_6 is inversion local mode (TROVE) quantum numbers. The mapping between these quantum numbers for a particular level also required knowledge of the energy value and symmetry, since multiple levels may be labelled with the same local mode quantum numbers. In these ambiguous cases, the symmetric modes quantum numbers n_1 and n_2 were chosen for the lower energies, and n_3 and n_4 with the higher, and that L_3 and L_4 increase proportionally with the energies, and are multiples of 3 in the case of A_1 or A_2 symmetries, or otherwise for the E-type symmetry. This mapping is performed by hand at the $J = 0$ stage of the calculation, and then propagated to $J > 0$.

The Einstein-A coefficient for a particular transition from the *initial* state i to the *final* state f is given by:

$$A_{if} = \frac{8\pi^4 \tilde{\nu}_{if}^3}{3h}(2J_i+1) \sum_{A=X,Y,Z} |\langle \Psi^f | \bar{\mu}_A | \Psi^i \rangle|^2, \quad (19)$$

where h is Planck's constant, $\tilde{\nu}_{if}$ is the wavenumber of the line, ($hc\tilde{\nu}_{if} = E_f - E_i$), J_i is the rotational quantum number for the initial state, Ψ^f and Ψ^i represent the TROVE eigenfunctions of the final and initial states respectively, $\bar{\mu}_A$ is the electronically averaged component of the dipole moment along the space-fixed axis $A = X, Y, Z$ (see also Yurchenko et al. (2005a)).

Table 7. Values of the partition function, Q, for different temperatures, T. The degree of convergence is specified by $Q_{J_{130}} - Q_{J_{129}}/Q_{J_{130}} \times 100$.

T (K)	Q	Degree of Convergence (%)
298.15	7908.906	6.27×10^{-6}
473.15	26065.642	8.50×10^{-4}
573.15	48007.866	3.62×10^{-3}
673.15	85016.645	9.99×10^{-3}
773.15	145389.574	2.12×10^{-2}
1000	437353.233	

In order to calculate the absorption intensity for a given temperature T only five quantities are required (all provided by UYT2), the transition wavenumber $\tilde{\nu}_{if}$, the Einstein coefficient A_{if}, the lower (initial) state energy term value $\tilde{E}_i$, the total degeneracy of the upper (final) state $g_f = g_{\rm ns} J_f(J_f + 1)$, and the partition function $Q(T)$, as given by

$$I(f \leftarrow i) = \frac{A_{if}}{8\pi c} \frac{g_f}{Q} \tilde{\nu}_{if}^2 \exp\left(-\frac{c_2 \tilde{E}_i}{T}\right) \left[1 - \exp\left(\frac{-c_2 \tilde{\nu}_{if}}{T}\right)\right], \quad (20)$$

where c_2 is the second radiation constant, $g_{\rm ns}$ is the nuclear spin statistical weight factor ($g_{\rm ns} = 1$ for $^{32}S^{16}O_3$), c is the speed of light. The partition function Q is given by:

$$Q = \sum_i g_i \exp\left(\frac{-c_2 \tilde{E}_i}{T}\right). \quad (21)$$

For a line list to be suitable for modelling spectra at a certain temperature it is necessary for the partition function, Q, to be converged at this temperature. This is equivalent to stating that all energy levels that are significantly populated at the given temperature, T, must be considered. This convergence gives a metric upon which line list completeness can be gauged (Neale et al. 1996).

Figure 4 shows convergence of the partition function with $J_{\rm max}$ for different temperatures, T. Upon inspection, the value of Q is adequately converged at $J = 130$ for $T \leq 800$ K. Table 7 shows the final values of Q obtained for selected temperature alongside their estimated degree of convergence. As can be seen, the value of $Q = 7908.906$ at $T = 298.15$ K calculated from UYT2 is in agreement with the value of $Q = 7908.266$ obtained from UYT.

For the purposes of determining completeness of the line list, it is more appropriate to view the convergence of Q as a function of an energy cut-off, $E_{\rm max}$. This is also shown in Figure 4, from where it is clear from that imposing this limit will have a non-negligible effect on a spectral simulation at $T = 773.15$ K, in particular; since the partition function is not fully converged at $E_{\rm max} = 4000$ cm^{-1} it is expected that levels with energies above this value will also be populated to some extent. This would be manifest as certain lines being missing from the spectrum, where transitions from levels contributing with some significance to the partition function are not included. Similarly, the truncation of calculations at $J = 130$ means that a number of potentially contributing energy levels are omitted from the partition sum at $T = 773.15$ K; at $J = 130$ the lowest energy lies around 4000 cm^{-1}. This means that the high-T partition function obtained will be slightly lower than the fully converged value.

It is possible to quantify the completeness of the line list

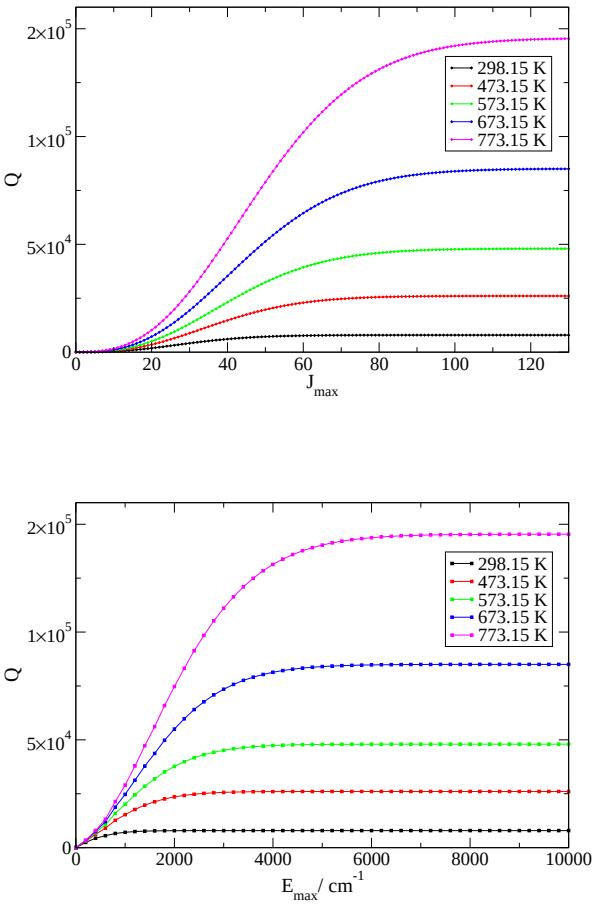

Figure 4. Convergence of partition function at different temperatures as a function of $J_{\rm max}$ (upper) and $E_{\rm max}$ (lower). The partition function increases monotonically with temperature.

by assuming that the value of Q at $J = 130$ is close enough to the 'true' value of the partition function at the given temperature. Figure 5 shows the ratio of the value of the partition function at the 4000 cm^{-1} cut-off and the assumed total partition function, $Q_{\rm Total}$. At $T = 773.15$ K, the line list is roughly 90% complete. In reality, this is an upper limit due to the fact that there is a slight underestimation of $Q_{\rm Total}$ at this temperature. However, the contribution from the missing energies with $J > 130$, which all lie above 4000 cm^{-1}, can be estimated to be small enough not to affect $Q_{\rm Total}$ by more than 1% below $T = 800$ K.

5 INTENSITY COMPARISONS

UYT (Underwood et al. 2013) made extensive intensity comparisons with the available, room temperature, high resolution, infrared spectra due to Maki *et al.*; in general finding good agreement. However, these experimental spectra are not absolute so the comparison is only for relative intensities. A comparison of the intensities predicted by the UYT and UYT2 line lists are summarised in Table 8. This comparison essentially shows that UYT2 reproduces the band

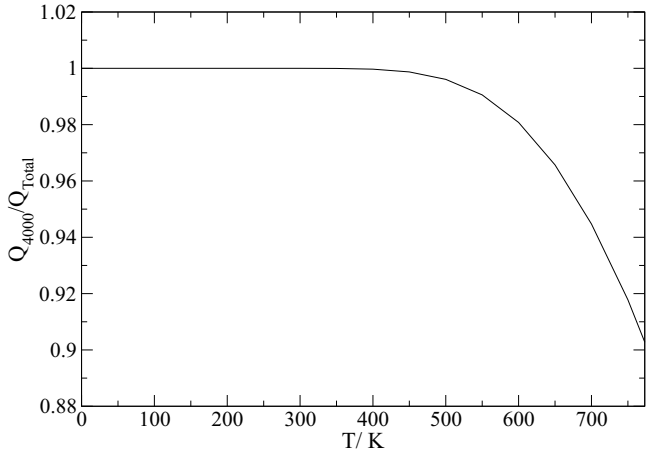

Figure 5. Ratios of Q_{4000} to the assumed converged values $Q_{\rm Total}$ as a function of temperature.

Table 8. Comparison of calculated band intensities in cm/molecule$\times 10^{-18}$. Units are given in 10^{-18} cm molecule^{-1}.

Band	Band Intensity	
	UYT	UYT2
$2\nu_2$ - ν_2	0.66	0.62
ν_2	3.71	3.39
ν_2 + ν_4 -ν_4	0.58	0.54
ν_4	5.95	5.37
$2\nu_4^{(l_4=0)}$ - ν_4	0.41	0.44
ν_2 + ν_4 - ν_2	0.53	0.49
$2\nu_4^{(l_4=2)}$ - ν_4	0.87	1.17
ν_1 - ν_4	0.10	0.22
ν_3	44.44	43.21
$2\nu_3^{(l_3=2)} - \nu_0$	0.12	0.11

intensities of UYT, showing that adjusting PES does not significantly alter the computed intensities, as has occasionally been found to happen (Al-Refaie et al. 2015b).

Since the comparison with the data of Maki *et al.* is only able to provide a measure of the quality of relative intensities within a particular band, an absolute intensity comparison is highly desirable. The new measured temperature-dependent DTU SO_3 cross section data plus the room-temperature cross sections in the PNNL (Pacific Northwest National Laboratory) database (Sharpe et al. 2004) provide this possibility. For both data sets there are discernible spectral features across four separate regions and it should be possible to make a semiquantitative analysis by comparing integrated intensities across a given spectral window. To make this comparison cross sections were generated from UYT2 using the ExoCross tool (Hill et al. 2013; Tennyson et al. 2016).

Figure 6 shows comparisons between recorded cross sections from PNNL at 298.15 K (25°C) and resolution 0.112 cm^{-1}, compared with simulated cross sections using the full UYT2 line list, based on a Gaussian profile of HWHM = 0.1 cm^{-1}. Figure 7 gives a similar comparison for the $\nu_1 + \nu_3$ and $2\nu_3$ bands.

Figure 8 shows a comparison of the the ν_2 and ν_4 complex and the ν_3 band between cross sections recorded for SO_3 at 573.15 K (300°C) and those simulated using the UYT2 line list, based on a Gaussian profile of HWHM = 0.25 cm^{-1}, this value is the one which gives the best representation of

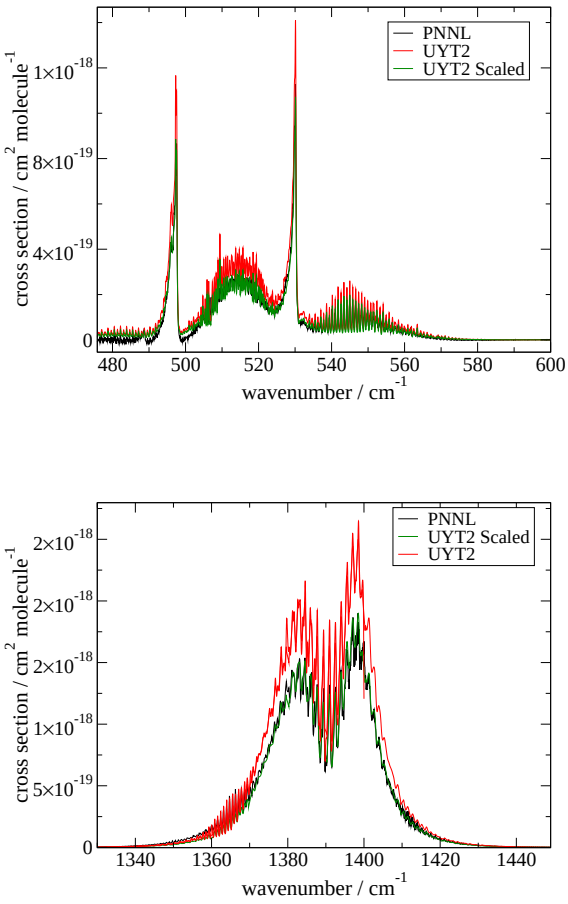

Figure 6. Comparisons of the ν_2 and ν_4 bands (upper) and the ν_3 band (lower) for PNNL (Sharpe et al. 2004) and simulated cross sections at T = 298.15 K.

the experimental spectra. In practice, the integrated intensity across the spectral region is largely independent of the HWHM value used. Figure 9 shows the same comparison for the $\nu_1 + \nu_3$ band, which appears in a noisier region of the spectrum, and is also disturbed by a strong, foreign absorption feature resulting from the presence of CO_2. There is no data at T = 573.15 K for the $2\nu_3$ band due to noise contamination in the associated spectral region. Measurements of SO_3 were also made for 773.15 K (500°C), however it has not been possible to generate accurate experimental cross section values due to difficulties in estimating the concentration within the gas flow cell. The integrated absorption cross sections reconstructed from the experimental data at 500°C are larger values than those at lower temperatures (< 500°C) suggesting non-conservation of the integrals over the various SO_3 bands. This might be explained by other, probably hetero-phase processes, which give rise to different SO_3 concentrations than one would expect from the assumption made that all SO_2 consumed in the reaction (8) gives raise of SO_3.

The comparisons reveals that although band positions and features are fairly well represented, there is a clear tendency for the UYT2 data to overestimate the line inten-

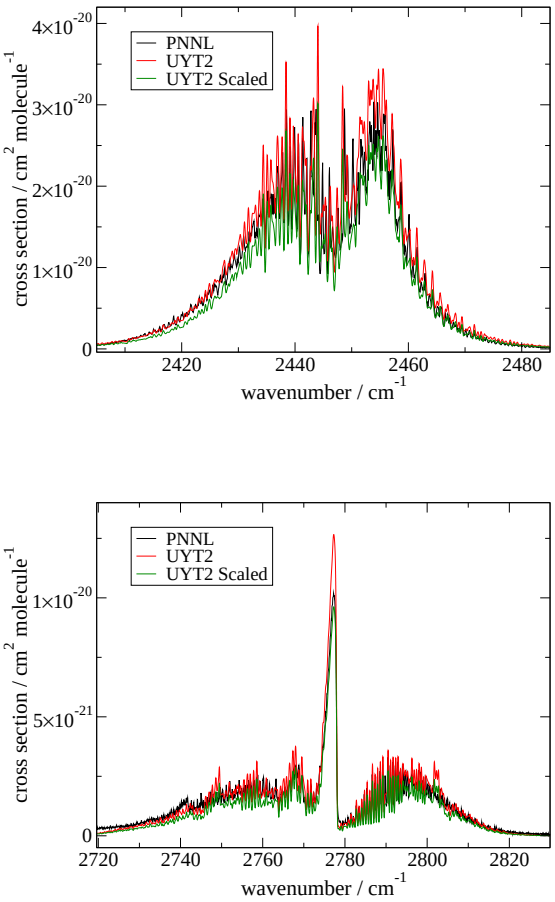

Figure 7. Comparisons of the $\nu_1 + \nu_3$ bands (upper) and the $2\nu_3$ band (lower) for PNNL (Sharpe et al. 2004) and simulated cross sections at $T = 298.15$ K.

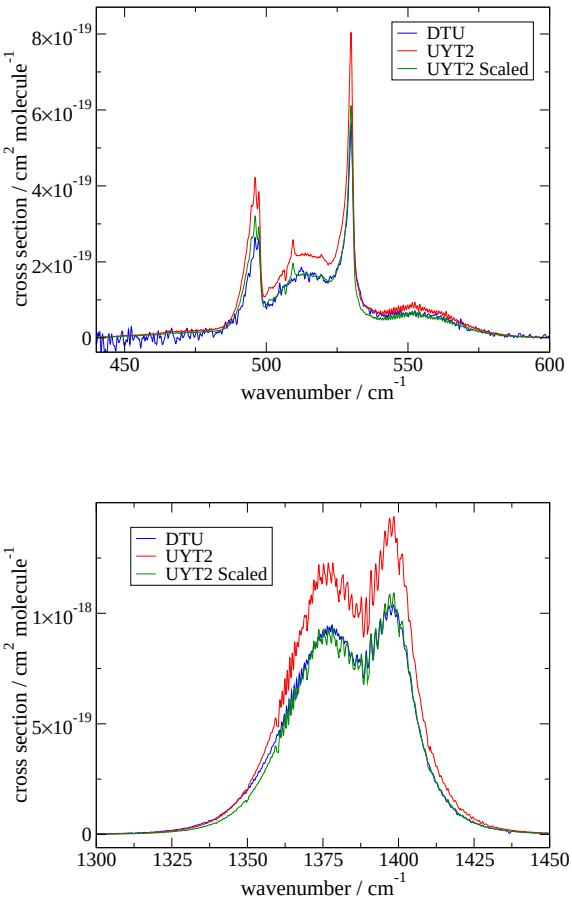

Figure 8. Comparisons of the ν_2 and ν_4 bands (upper) and the ν_3 band (lower) for experimentally obtained (this work) and simulated cross sections at $T = 573.15$ K.

sities for both temperatures considered. In our experience of computing *ab initio* intensities it is common for whole bands to have intensities which are over/underestimated by a constant factor (Lodi et al. 2008). However, we have not previously encountered a situation where the intensities of all the bands are shifted by a similar amount. There are a number of possibilities that could explain such a discrepancy. Firstly, it is possible that the experimental cross sections may be underestimated due to an overestimate of the SO_3 abundance; the calculation of cross sections requires the knowledge of the species concentration within the length of the absorption cell (Barton et al. 2015). However, the fact that measurements at room-temperature performed at DTU corroborate the PNNL data, and that similar discrepancies are observed for both data sets suggests that this is not the case. In this context it is worth noting that a similar comparison for SO_2 yields good agreement between measure and *ab initio* absolute cross sections (Underwood et al. 2016).

A second possible source of disagreement could be convergence issues with the partition function. Since the calculated intensities given by Eq. (20) depend on the scaling factor $Q(T)$ the incorrect computation of this value at the given temperature will lead to inaccurate values of absolute

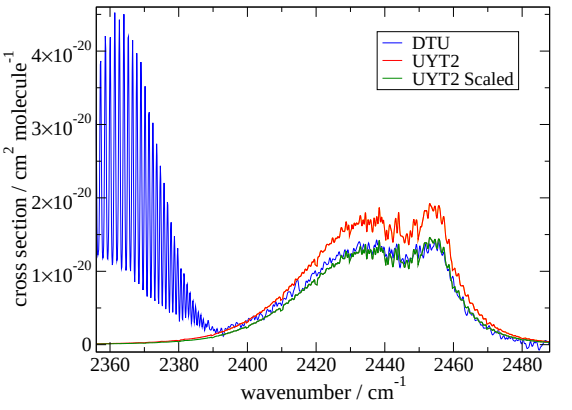

Figure 9. Comparisons of the $\nu_1 + \nu_3$ bands for experimental (this work) and simulated cross sections at $T = 573.15$ K.

intensity. The difference in integrated cross section intensities observed suggest that, if the calculated value of $Q(T)$ is incorrect, then it is smaller than the 'true' value, since the theoretical cross sections are more intense than the experimentally observed values. This scenario can also be ruled out, due to two reasons. First, the agreement between $Q(T)$ for both UYT and UYT2 is very good at $T = 298.15$ K, where they are both adequately converged; the increased basis set size underlaying the UYT2 calculations would undoubtedly account for any missing rovibrational energies in UYT. Secondly, and perhaps more interestingly, the analysis of several bands across different temperatures shows the cross section discrepancies to be almost independent of the value of T (see below). This would not be expected if $Q(T)$ were the source of the disagreement, since partition sums can be expected to converge differently as a function of temperature.

This heavily implies that the problem lies with the DMS defects are by no means unknown (Al-Refaie et al. 2015b; Pavlyuchko et al. 2015a; Azzam et al. 2015), despite previous experience of obtaining accurate *ab initio* dipole surfaces (Lodi et al. 2011; Polyansky et al. 2015). We therefore undertook a small series of new *ab initio* calculations to see if we could identify the source of this problem. These calculations were all performed with MOLPRO (Werner et al. 2012) at the CCSD(T) level using finite differences. First we compared the original CCSD(T)-F12b with triple-ζ basis sets (aug-cc-pVTZ-F12 on O and aug-cc-pV(T+d)Z-F12 on S) results with calculations performed at the more traditional CCSD(T) with the same basis sets. The results were very similar suggesting that use of F12b what neither the cause of the problem nor was it providing improved convergence. Second we repeated the CCSD(T) using a larger quadrupole-zeta basis set (aug-cc-pVQZ-F12 on O and aug-cc-pV(Q+d)Z-F12 on S). The dipoles computed at this level proved to be somewhat smaller suggesting that the UYT DMS suffers from a lack of convergence in the one-particle basis set. Further work on this problem is left to future work. Here we adopt the more pragmatic approach of scaling our computed intensities.

It is not easy to make a rigorous analysis based on cross section data available for SO_3, as it is not immediately obvious what the contributions are from individual lines. In addition to this, both data sets contain varying degrees of noise within certain spectral regions, with the region around the ν_3 band generally providing the best signal. Pavlyuchko et al. (2015a) performed a fit of their DMS based on experimental intensity data for nitric acid, to better improve simulated intensities. The lack of absolute intensity measurements for SO_3, coupled with the expensive computational demands of the line list calculation make this particularly difficult to perform here. Nevertheless, the best approach has been to compare integrated band intensities across fixed spectral windows to obtain scaling parameters for the each band. Table 9 summarises the ratios of integrated intensities between simulated and recorded cross sections for some available bands. These were obtained by explicit numerical integration over the wavenumber range of the corresponding regions.

For most bands there appears to be a fairly consistent shift in intensity values across different temperatures, however the overtone bands for $T = 298.15$ K suggest otherwise.

Table 9. Intensities integrated over the corresponding band region for observed and calculated (UYT2) cross sections as a function of temperature, T. Intensity units are given in 10^{-18} cm molecule^{-1}.

T (K)	Band	Integrated Intensity Obs.	UYT2	Obs./UYT2
298.15	ν_2 & ν_4	9.95	13.13	0.76
	ν_3	46.78	60.38	0.77
	$\nu_1 + \nu_3$	0.71	0.82	0.87
	$2\nu_3$	0.15	0.16	0.97
573.15	ν_2 & ν_4	10.26	13.53	0.76
	ν_3	46.79	59.62	0.78
	$\nu_1 + \nu_3$	0.69	0.87	0.79

The differences are quite subtle; for example, while the $2\nu_3$ band has almost perfect agreement in integrated intensity across the band, the central Q-branch peak is not well represented by the UYT2 cross sections. On the other hand, the DTU data at 573.15 K for the $\nu_1 + \nu_3$ band exhibits the same general shift as the ν_2, ν_3 and ν_4 bands when care is taken exclude the intensity due to contamination in the integration, but the same is not true at room-temperature. The PNNL room-temperature cross sections are presented as a composite spectrum created from 8 individual absorbance spectra taken at various different pressures using both a mid-band MCT and wide-band-MCT detector, and uncertainties in intensity are listed as 10%. The measurements at DTU were performed several times and over different years, when the cell was used for other measurements. The data however are well-reproducible. Up to 400°C agreement in integrated absorption cross sections between DTU and PNNL is from 0 % to 13 % for strongest bands that is the same order as PNNL's uncertainties in bands intensity. If the scaling factors for the two overtone bands at room-temperature are ignored, then the remaining factors may be averaged and applied to all simulated cross sections. This gives an average scaling factor of 0.76. The assumption made here is that the apparent better agreement in the room-temperature intensities for the $\nu_1 + \nu_3$ and $2\nu_3$ are 'accidental', while the wide, coverage-consistent high-temperature cross sections provide a more accurate description of the differences. Previous experience suggests that an *ab initio* DMS is more likely to overestimate rather than underestimate intensities (Schwenke & Partridge 2000; Tennyson 2014; Azzam et al. 2015). Without extra experimental data for more bands at different temperatures it is difficult to ascertain whether the intensity overestimates seen here are consistent for all bands or vary with different vibrational transitions.

Figures 6 and 7 show the various bands at room-temperature, with computed cross sections multiplied by the averaged scaling factor. Figures 8 and 9 show the same for $T = 573.15$ K, which improve the simulated cross sections, and demonstrate the implied temperature independent nature of the discrepancy. As can be seen in Figure 7, using the averaged scaling factor (obtained from excluding the individual $\nu_1 + \nu_3$ and $2\nu_3$ Obs./UYT2 ratios) improves the reproduction of the central band peak, though the P-branch does show some intensity differences. This appears to be common for multiple bands and is possibly due to our neglecting of pressure broadening when generating the cross sections.

Figure 10 shows the cross sections calculated over the

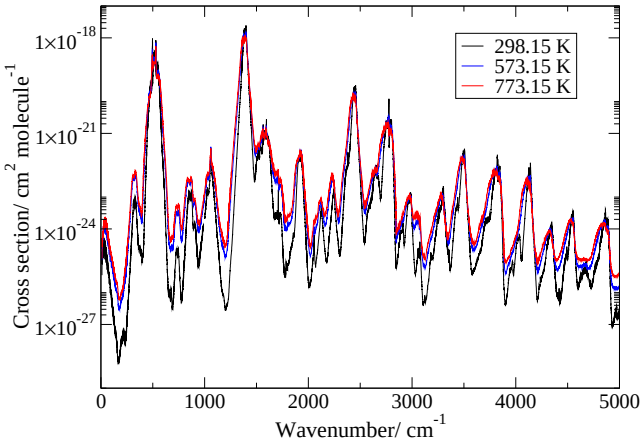

Figure 10. Overview of the simulated cross sections using UYT2, at T = 298.15, 473.15 and 773.15 K, with a Gaussian profile of HWHM = 0.25 cm^{-1}. The dips in the cross sections are progressively smoothed out with increasing temperature. For higher temperatures, the region beyond 4500 cm^{-1} appears anomalous, and should be treated with caution.

entire spectral range of $0 < \nu \leq 5000$ cm^{-1}, using a Gaussian profile of HWHM = 0.25 cm^{-1}, for a number of different temperatures. All simulated cross sections have been multiplied by the average scaling factor of 0.76. As can be seen, the region beyond 4500 cm^{-1} shows some anomalies for higher temperatures, for this reason it is recommended that this region be treated with caution.

6 CONCLUSION

The UYT2 line list contains 21 billion transitions, and a total of 18 million energy levels below 10 000cm^{-1}. This provides an improvement upon the initial room-temperature line list, UYT, in terms of both line positions and temperature coverage. Table 1 provides a measure of the improvement introduced by the PES refinement present in the UYT2 line list. The total RMS deviation for the bands included in the potential adjustment is 1.35 cm^{-1}, compared to 3.23 cm^{-1} for the unrefined PES of UYT. The majority of simulated line positions across these bands is improved by an order of magnitude.

It is difficult to ascertain the overall quality of the *ab initio* DMS used in the production of line intensities. However comparing with newly available cross section data at two different temperatures heavily suggests that the DMS used in the calculation of intensities is slightly overestimated, causing an apparently constant shift in all intensity values. The evidence suggesting this temperature- and band-independent scaling factor is certainly not conclusive, and one may wish to take care in which scaling factor to use for each band. In particular, bands for which there are no experimental intensity data available can not be considered to be truly represented well in UYT2 and the lack of exhaustive absolute intensity knowledge for SO_3 limits our ability to effectively correct for the disagreements observed. Nevertheless it is hoped that the scaling factor improves the *ab initio* intensity values produced in the UYT2 line list. Further work, probably starting with a systematic *ab initio* study of the type recently performed for H_2S by Azzam et al. (2015), is required in order to fully investigate the source of this discrepancy. An experimental determination of individual line intensities would also be extremely helpful.

The increased size of the basis set, the computation of rovibrational energies up to $J = 130$, and the increased spectral range of line strength calculations allows for UYT2 to be used in the simulation of spectra between $0 < \nu \leq 5000$ cm^{-1}, with approximately 90% completion at T = 773.15 K (500 C), however calculated cross sections for the region beyond 4500 cm^{-1} should be treated cautiously, and will have to be further investigated. Given that this is the largest data set of its kind for SO_3, it is recommended that UYT2 be used in the production of cross sections at room-temperature, and up to T = 773.15 K, for both astronomical and other applications.

The UYT2 line list contains 21 billion transitions. This makes it use in radiative transport modelling computationally challenging. Work on an even larger methane line list (Yurchenko et al. 2016) suggests that it should be possible to split the list into a temperature-dependent but pressure-independent, background cross section which is used to augment a hugely reduced list of stong line whose profiles are treated in detail. This idea will be explored further in the future.

ACKNOWLEDGEMENTS

This work was supported by Energinet.dk project 2010-1-10442 “Sulfur trioxide measurement technique for energy systems” and the ERC under the Advanced Investigator Project 267219. It made use of the DiRAC@Darwin HPC cluster which is part of the DiRAC UK HPC facility for particle physics, astrophysics and cosmology and is supported by STFC and BIS as well as the Emerald Computing facility funded by EPSRC. We thank Cheng Liao and the SGI team for providing the Plasma diagonaliser and DiRAC project at Cambridge for assistance in running our jobs.

REFERENCES

Adande G. R., Edwards J. L., Ziurys L. M., 2013, ApJ, 778, 22
Adler T. B., Knizia G., Werner H.-J., 2007, J. Chem. Phys., 127, 221106
Al-Refaie A. F., Ovsyannikov R. I., Polyansky O. L., Yurchenko S. N., Tennyson J., 2015a, J. Mol. Spectrosc., 318, 84
Al-Refaie A. F., Yurchenko S. N., Yachmenev A., Tennyson J., 2015b, MNRAS, 448, 1704
Al-Refaie A. F., Tennyson J., Yurchenko S. N., 2016, Comput. Phys. Commun.
Anderson E., et al., 1999, LAPACK Users’ Guide, third edn. Society for Industrial and Applied Mathematics, Philadelphia, PA
Azzam A. A. A., Lodi L., Yurchenko S. N., Tennyson J., 2015, J. Quant. Spectrosc. Radiat. Transf., 161, 41
Barber J., Chrysostom E. T. H., Masiello T., Nibler J. W., Maki A., Weber A., Blake T. A., Sams R. L., 2002, J. Mol. Spectrosc., 216, 105
Barton E. J., Yurchenko S. N., Tennyson J., Clausen S., Fateev A., 2015, J. Quant. Spectrosc. Radiat. Transf., 167, 126
Belloche A., Müller H. S. P., Menten K. M., Schilke P., Comito C., 2013, A&A, 559, A47
Belyaev D. A., et al., 2012, Icarus, 217, 740

Burkholder J. B., McKeen S., 1997, Geophys. Res. Lett., 24, 3201
Calvert J. G., Lazrus A., Kok G. L., Heikes B. G., WalegaAL J. G., Lind J., Cantrell C. A., 1985, Nature, 317, 27
Chrysostom E. T. H., Vulpanovici N., Masiello T., Barber J., Nibler J. W., Weber A., Maki A., Blake T. A., 2001, J. Mol. Spectrosc., 210, 233
Craig R. A., Reynolds R. T., Ragent B., Carle G. C., Woeller F., Pollack J. B., 1983, Icarus, 53, 1
Dorney A. J., Hoy A. R., Mills I. M., 1973, J. Mol. Spectrosc., 45, 253
Down M. J., Hill C., Yurchenko S. N., Tennyson J., Brown L. R., Kleiner I., 2013, J. Quant. Spectrosc. Radiat. Transf., 130, 260
Fajans E., Goodeve C. F., 1936, Trans. Faraday Soc., 32, 511
Feynman R. P., 1939, Phys. Rev., 56, 340
Flament J. P., Rougeau N., Tadjeddine M., 1992, Chem. Phys., 167, 53
Fleig D., Vainio E., Andersson K., Brink A., Johnsson F., Hupa M., 2012, Energy Fuels, 26, 5537
Grosch H., Fateev A., Clausen S., 2015a, J. Quant. Spectrosc. Radiat. Transf., 154, 28
Grosch H., Sarossy Z., Fateev A., Clausen S., 2015b, J. Quant. Spectrosc. Radiat. Transf., 156, 17
Grosch H., Fateev A., Nielsen K. L., Clausen S., 2013, J. Quant. Spectrosc. Radiat. Transf., 130, 392
Hieta T., Merimaa M., 2014, Appl. Phys B, 117, 847
Hill C., Yurchenko S. N., Tennyson J., 2013, Icarus, 226, 1673
Huang X., Schwenke D. W., Lee T. J., 2014, J. Chem. Phys., 140, 114311
Huang X., Schwenke D. W., Lee T. J., 2016, J. Mol. Spectrosc., 311, 19
Kaldor A., Maki A. G., Dorney A. J., Mills I. M., 1973, J. Mol. Spectrosc., 45, 247
Khayat A. S., Villanueva G. L., Mumma M. J., Tokunaga A. T., 2015, Icarus, 253, 130
Kolb C. E., Jayne J. T., Worsnop D. R., 1994, J. Am. Chem. Soc., 116, 10314
Kurzak J., et al., 2013, Multicore Computing: Algorithms, Architectures, and Applications, p. 119
Leroy B., Le Bras G., Rigaud P., 1981, Annales de Geophysique, 37, 297
Lodi L., Tennyson J., 2010, J. Phys. B: At. Mol. Opt. Phys., 43, 133001
Lodi L., et al., 2008, J. Chem. Phys., 128, 044304
Lodi L., Tennyson J., Polyansky O. L., 2011, J. Chem. Phys., 135, 034113
Maki A., et al., 2001, J. Mol. Spectrosc., 210, 240
Maki A., et al., 2004, J. Mol. Spectrosc., 225, 109
Martin J. M. L., 1999, Spectrochimica Acta A, 55, 709
Martin J. M. L., Kesharwani M. K., 2014, J. Chem. Theor. Comput., 10, 2085
Martin S., Mauersberger R., Martin-Pintado J., Garcia-Burillo S., Henkel C., 2003, A&A, 411, L465
Martin S., Martin-Pintado J., Mauersberger R., Henkel C., Garcia-Burillo S., 2005, ApJ, 620, 210
Meyer V., Sutter D. H., Dreizler H., 1991, Z. Naturforsch. A, 46, 710
Michaud J. P., Krupitsky D., Grove J. S., Anderson B. S., 2005, Neurotoxicology, 26, 555
Na C. Y., Esposito L. W., Skinner T. E., 1990, J. Geophys. Res., 95, 7485
Neale L., Miller S., Tennyson J., 1996, ApJ, 464, 516
Ortigoso J., Escribano R., Maki A. G., 1989, J. Mol. Spectrosc., 138, 602
Pavlyuchko A. I., Yurchenko S. N., Tennyson J., 2015a, J. Chem. Phys., 142, 094309
Pavlyuchko A. I., Yurchenko S. N., Tennyson J., 2015b, MNRAS, 452, 1702
Petuchowski S. J., Bennett C. L., 1992, ApJ, 391, 137
Polyansky O. L., Bielska K., Ghysels M., Lodi L., Zobov N. F., Hodges J. T., Tennyson J., 2015, Phys. Rev. Lett., 114, 243001
Rawlins W. T., Hensley J. M., Sonnenfroh D. M., Oakes D. B., Allen M. G., 2005, Appl. Optics, 44, 6635
Rothman L. S., et al., 2013, J. Quant. Spectrosc. Radiat. Transf., 130, 4
Schwenke D. W., Partridge H., 2000, J. Chem. Phys., 113, 6592
Sharpe S. W., et al., 2003, J. Mol. Spectrosc., 222, 142
Sharpe S. W., Johnson T. J., Sams R. L., Chu P. M., Rhoderick G. C., Johnson P. A., 2004, Appl. Spectrosc., 58, 1452
Sousa-Silva C., Yurchenko S. N., Tennyson J., 2013, J. Mol. Spectrosc., 288, 28
Sousa-Silva C., Al-Refaie A. F., Tennyson J., Yurchenko S. N., 2015, MNRAS, 446, 2337
Srivastava R., Miller C., Erickson C., Jambheka R., 2004, J. Air Waste Management Assoc., 54:6, 750
Tennyson J., 2014, J. Mol. Spectrosc., 298, 1
Tennyson J., Yurchenko S. N., 2012, MNRAS, 425, 21
Tennyson J., Hill C., Yurchenko S. N., 2013, in 6^{th} international conference on atomic and molecular data and their applications ICAMDATA-2012. AIP, New York, pp 186–195, doi:10.1063/1.4815853
Tennyson J., et al., 2016, J. Mol. Spectrosc.
Underwood D. S., 2016, PhD thesis, University College London
Underwood D. S., Tennyson J., Yurchenko S. N., 2013, Phys. Chem. Chem. Phys., 15, 10118
Underwood D. S., Yurchenko S. N., Tennyson J., Jensen P., 2014, J. Chem. Phys., 140, 244316
Underwood D. S., Tennyson J., Yurchenko S. N., Huang X., Schwenke D. W., Lee T. J., Clausen S., Fateev A., 2016, MNRAS
Vahedpour M., Goodarzi M., Hajari N., Nazari F., 2011, Structural Chemistry, 22, 817
Visscher C., Lodders K., Fegley Jr. B., 2006, ApJ, 648, 1181
Werner H.-J., Knowles P. J., Knizia G., Manby F. R., Schütz M., 2012, WIREs Comput. Mol. Sci., 2, 242
Whitehill A. R., Xie C., Hu X., Xie D., Guo H., Ono S., 2013, Proc. Nat. Acad. Sci., 110, 17697
Yachmenev A., Yurchenko S. N., Jensen P., Thiel W., 2011, J. Chem. Phys., 134, 11
Yurchenko S. N., Tennyson J., 2014, MNRAS, 440, 1649
Yurchenko S. N., Thiel W., Carvajal M., Lin H., Jensen P., 2005a, Adv. Quant. Chem., 48, 209
Yurchenko S. N., Carvajal M., Jensen P., Lin H., Zheng J. J., Thiel W., 2005b, Mol. Phys., 103, 359
Yurchenko S. N., Thiel W., Jensen P., 2007, J. Mol. Spectrosc., 245, 126
Yurchenko S. N., Barber R. J., Yachmenev A., Thiel W., Jensen P., Tennyson J., 2009, J. Phys. Chem. A, 113, 11845
Yurchenko S. N., Barber R. J., Tennyson J., Thiel W., Jensen P., 2011, J. Mol. Spectrosc., 268, 123
Yurchenko S. N., Amundsen D. S., Tennyson J., 2016, A&A
Zak E., Tennyson J., Polyansky O. L., Lodi L., Tashkun S. A., Perevalov V. I., 2016, J. Quant. Spectrosc. Radiat. Transf., 177, 31
Zhang X., Liang M.-C., Montmessin F., Bertaux J.-L., Parkinson C., Yung Y. L., 2010, Nat. Geosci., pp 834–837
Zhang X., Liang M. C., Mills F. P., Belyaev D. A., Yung Y. L., 2012, Icarus, 217, 714